Letter | Editors' Suggestion

Relating spin-polarized STM imaging and inelastic neutron scattering in the van der Waals ferromagnet Fe_3GeTe_2

Christopher Trainer,[1] Olivia R. Armitage,[1] Harry Lane,[2,3,4] Luke C. Rhodes,[1] Edmond Chan,[2,5] Izidor Benedičič,[1] J. A. Rodriguez-Rivera,[6,7] O. Fabelo,[5] Chris Stock,[2] and Peter Wahl[1]

[1]*SUPA, School of Physics and Astronomy, University of St. Andrews, North Haugh, St. Andrews, Fife, KY16 9SS, United Kingdom*
[2]*School of Physics and Astronomy, University of Edinburgh, Edinburgh EH9 3JZ, United Kingdom*
[3]*School of Chemistry and Centre for Science at Extreme Conditions, University of Edinburgh, Edinburgh EH9 3FJ, United Kingdom*
[4]*ISIS Pulsed Neutron and Muon Source, STFC Rutherford Appleton Laboratory, Harwell Campus, Didcot, Oxon, OX11 0QX, United Kingdom*
[5]*Institute Laue-Langevin, 6 rue Jules Horowitz, Boite Postale 156, 38042 Grenoble Cedex 9, France*
[6]*NIST Center for Neutron Research, National Institute of Standards and Technology, Gaithersburg, Maryland 20899, USA*
[7]*Department of Materials Science and Engineering, University of Maryland, College Park, Maryland 20742, USA*

(Received 2 March 2022; revised 8 June 2022; accepted 27 July 2022; published 15 August 2022)

Van der Waals (vdW) ferromagnets have enabled the development of heterostructures assembled from exfoliated monolayers with spintronics functionalities, making it important to understand and ultimately tune their magnetic properties at the microscopic level. Information about the magnetic properties of these systems comes, so far, largely from macroscopic techniques, with little being known about the microscopic magnetic properties. Here, we combine spin-polarized scanning tunneling microscopy and quasiparticle interference imaging with neutron scattering to establish the magnetic and electronic properties of the metallic vdW ferromagnet Fe_3GeTe_2. By imaging domain walls at the atomic scale, we can relate the domain wall width to the exchange interaction and magnetic anisotropy extracted from the magnon dispersion as measured in inelastic neutron scattering, with excellent agreement between the two techniques. From comparison with density functional theory calculations we can assign the quasiparticle interference to be dominated by spin-majority bands. We find a dimensional dichotomy of the bands at the Fermi energy: bands of minority character are predominantly two-dimensional in character, whereas the bands of majority character are three-dimensional. We expect that this will enable new design principles for spintronics devices.

DOI: 10.1103/PhysRevB.106.L081405

I. INTRODUCTION

The discovery of ferromagnetic van der Waals (vdW) materials has enabled the possibility of manufacturing spintronics devices from vdW heterostructures [1]. Although, according to the Mermin-Wagner theorem, ferromagnetism should be unstable in two dimensions, recently a number of materials, including Fe_3GeTe_2, were shown to exhibit ferromagnetism down to the monolayer limit [2–4]. The evolution of its magnetic order from three to two dimensions is an interesting open question [5]. The study of magnetic properties in two-dimensional (2D) materials and at surfaces, however, is challenging. Conventional methods used to establish magnetic order parameters, such as neutron scattering, are not suitable for monolayer-thin samples and surfaces, at the same time, interesting new phenomena are expected in 2D magnetic systems [6]. In particular Fe_3GeTe_2 shows a surprising breadth of phenomena, including evidence for electronic correlation effects resulting in Kondo-lattice-like behavior [7] and a magnetic ground state that sensitively depends on the exact stoichiometry and concentration of iron in the samples [8,9]. Here, we use spin-polarized STM, quasiparticle interference imaging, and neutron scattering to elucidate the interplay between the bulk and surface magnetic order and the low-energy electronic structure of a quasi-2D ferromagnet. We identify two types of defects arising predominantly from Fe and Te vacancies, and show that quasiparticle scattering from these defects produces magnetic scattering dominated by the more 2D electronic bands around the Fermi level. Imaging of a domain wall and comparison of its profile with the exchange coupling J and magnetic anisotropy K obtained from inelastic neutron scattering of bulk Fe_3GeTe_2 reveals good agreement, with the evidence for a larger magnetic anisotropy and smaller exchange coupling in the surface layer.

II. RESULTS

A. Sample characterization

Fe_3GeTe_2 has a layered crystal structure with weak interlayer interactions and becomes ferromagnetic below $T = 230\,\mathrm{K}$ [10]. The material typically comes with an off-stoichiometry, where the iron concentration deviates from three due to vacancies and interstitial iron. The magnetic properties vary with the excess iron concentration [8]. Previous scanning tunneling microscope (STM) and angle-resolved photoemission spectroscopy (ARPES) investigations were interpreted as Kondo-lattice-like behavior [7]. The material cleaves easily between the $Fe_{3-y}GeTe_2$ layers, exhibiting a Te-terminated surface. We used single-crystal neutron

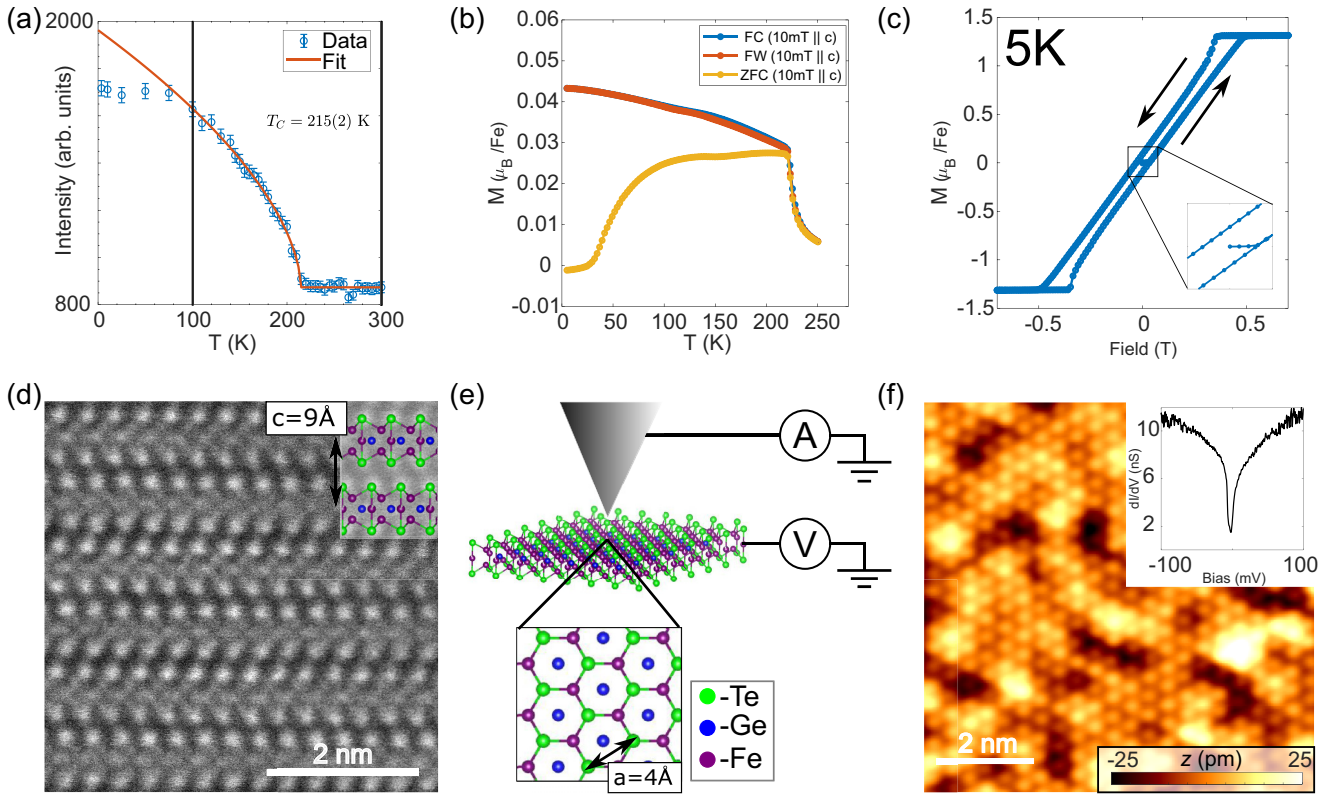

FIG. 1. Sample characterization. (a) Intensity of neutrons scattered at the atomic Bragg peak as a function of temperature. The signal will consist of the structural peak and the magnetic signal due to the ferromagnetic order. The red line represents a power-law fit to the data giving a ferromagnetic transition temperature of 215K. (b) Magnetization M of the Fe_3GeTe_2 crystal used for the STM measurements. Zero-field-cooled (ZFC), field-cooled (FC), and field-warmed (FW) measurements are shown. The transition temperature T_c is found to be $T_c = 218$ K and is extracted by fitting a Curie-Weiss law to the high temperature data. (c) A low-temperature magnetization M vs. field H loop recorded in the ferromagnetic phase. Inset: Close up of a 50 mT window around zero field. (d) TEM image of the layered structure of Fe_3GeTe_2. Inset: Side view of the crystal structure. (e) Schematic of the STM tunnel junction experimental setup. Inset: The Fe_3GeTe_2 crystal structure. (f) A topographic STM image of the Fe_3GeTe_2 surface ($V_s = 30$ mV, $I_s = 1$ nA). Inset: Typical STS spectrum recorded on the surface of Fe_3GeTe_2 ($V_s = 100$ mV, $I_s = 1$ nA).

diffraction to determine the crystal structure, and in particular, the exact stoichiometry of our samples, revealing an iron deficiency $y = 0.14$ (see Supplemental Material S2 [32]).

Magnetic characterization [Figs. 1(a) and 1(b)] reveals a behavior in field-cooled measurements consistent between the neutron scattering intensity of the Bragg peak and magnetization, as well as with previous reports [11]. We find the magnetic transition at about 220 K and a suppression of magnetization for zero-field-cooled measurements starting below 100 K, Fig. 1(b), indicating stabilization of a domain structure which results in zero net magnetization. In measurements of the magnetization M as a function of field H, shown in Fig. 1(c), we find magnetic hysteresis, as expected for a ferromagnet.

Cross-sectional TEM images [Fig. 1(d)] show the stacking sequence as expected from the crystal structure and the high quality of the samples, confirming the AB layer stacking. This type of stacking results in a Rashba-like band crossing at the K point and leads to the formation of topological line nodes [12].

Figure 1(e) shows the measurement set up for the STM measurement and expected surface termination. Topographic imaging of the Fe_3GeTe_2 surface [Fig. 1(f)] reveals a hexagonal lattice, which can be attributed to the uppermost Te lattice. The surface further exhibits a pronounced electronic inhomogeneity, which likely originates from the off-stoichiometry of the sample due to the iron deficiency. STS spectra show a pronounced gap around the Fermi level [inset of Fig. 1(f)].

To gain a better understanding of the inhomogeneity in our topographic images, we simulated STM images for different types of defects. Figure 2 shows density functional theory (DFT) calculations and measured topographic images for the clean surface and two types of defects, an iron vacancy and a tellurium vacancy. Comparison of the DFT calculations with the STM image for the clean surface [Figs. 2(a) to 2(c)] suggests that the atomic corrugation in the STM images is due to the surface tellurium lattice. A vacancy of a tellurium atom [as indicated in Fig. 2(d)] results in a clear triangular-like defect [Fig. 2(e)], which can be easily identified in the topographic image [Fig. 2(f)]. An Fe-vacancy, shown in Fig. 2(g), produces a more subtle depression of the local density of states, as shown in Fig. 2(h), which can nevertheless be easily identified in our STM topographies [Fig. 2(i)]. This depression in the density of states is likely responsible for the inhomogeneity in topographic images as shown in Fig. 1(b), and has been shown to be responsible for the lowering in T_c as a function of Fe deficiency [8]. Interestingly, within our ferromagnetic

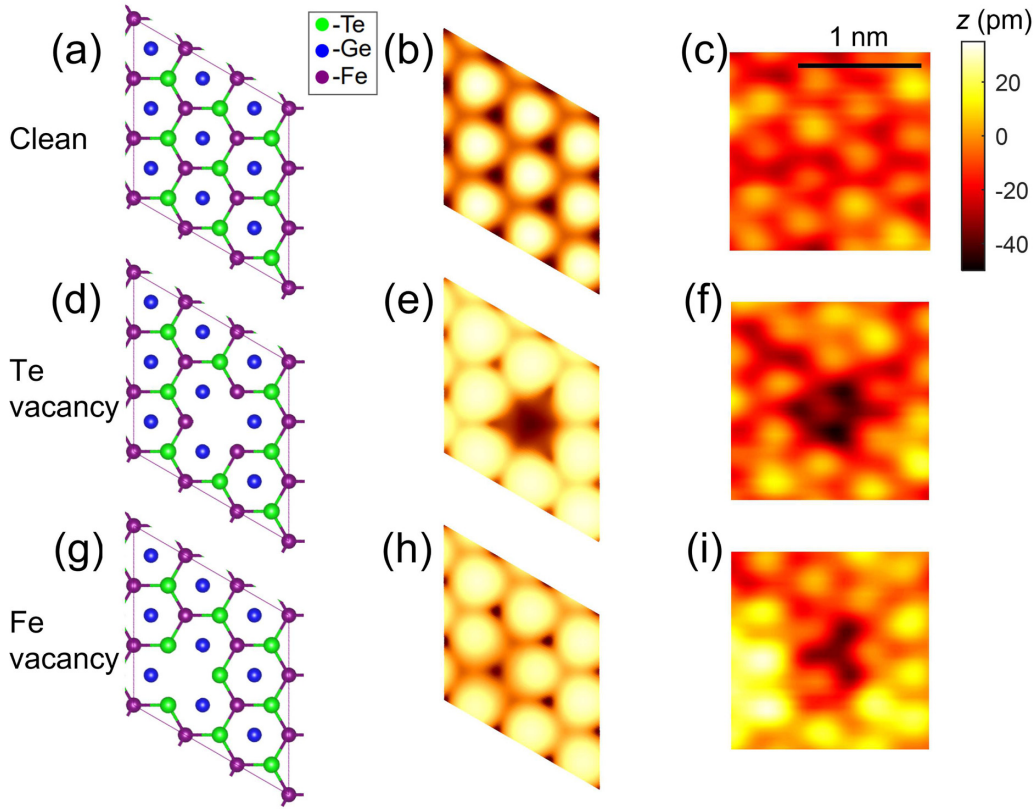

FIG. 2. Identification of defects. (a) Top view of a 3×3 supercell of a monolayer of Fe_3GeTe_2. (b) Simulated STM topography of the supercell in (a). (c) STM topography of a region of the Fe_3GeTe_2 surface containing no defects. (d) Top view of supercell in (a) with a Te atom removed. (e) Simulated STM topography of the supercell in (d). (f) STM topography of the Fe_3GeTe_2 surface, showing a Te-site defect. (g) Same supercell as in (a), with an Fe atom removed, corresponding to $y = 0.14$ (i.e., $Fe_{2.86}GeTe2$). (h) Simulated STM topography of the supercell in (g). (i) STM topography of the Fe_3GeTe_2 surface, showing an Fe-site defect. STM images (c), (f), and (i) taken with $V_s = 50\,\mathrm{mV}$, $I_s = 50\,\mathrm{pA}$. Simulated images (b), (e), and (h) calculated for constant current and $V_s = 100\,\mathrm{mV}$.

DFT calculations for a monolayer of Fe_3GeTe_2 in a 3×3 supercell, we find that the total magnetic moment per Fe atom is reduced by the presence of a defect (2.004 μ_B/Fe versus 2.123 μ_B/Fe without a defect, see the Supplementary Material S1 [32]). Previous studies by DFT showed that the presence of defects can also have dramatic consequences for the magnetic interlayer coupling [9].

B. Magnetic properties from STM and neutron scattering

We studied the magnetism in Fe_3GeTe_2 using neutron scattering and spin-polarized STM to establish a better understanding of its magnetic properties, and the effect of the vacuum interface which will become more important in the 2D limit.

Figure 3(a) shows the inelastic neutron data obtained from a single crystal, with a clear magnon dispersion in a cut through the (0,0,2) peak starting from about 1 meV. At long wavelengths, the magnetic excitations of an itinerant ferromagnet are well described by a model of localized magnetic moments [13]. To describe the spin-wave dispersion in Fe_3GeTe_2 at small $\mathbf{q}$, we use an effective 2D model of interacting Fe^{3+} ions on a honeycomb lattice with an easy-axis anisotropy

$$\mathcal{H} = J \sum_{\mathbf{r}}^{j\in\{0,1,2\}} \mathbf{S}_A(\mathbf{r}) \cdot \mathbf{S}_B(\mathbf{r}+\mathbf{a}_j) + K\left[\left(\hat{S}_A^z(\mathbf{r})\right)^2 + \left(\hat{S}_B^z(\mathbf{r})\right)^2\right]. \tag{1}$$

Here, J is the nearest-neighbor interaction, K the magnetic anisotropy, $\mathbf{S}_{A,B}$ is the spin operator acting on site A or B, and the vectors $\mathbf{a}_0 = (0,0)$, $\mathbf{a}_1 = (0,1)$, and $\mathbf{a}_2 = (1,1)$ span between the unit cells containing nearest-neighbor spins (in the $P6_3/mmc$ space group). We neglected further nearest neighbors since their effect in the limit of small $|\mathbf{q}|$ is a simple renormalization of the spin-wave velocity and anisotropy gap. Out of plane couplings in materials where the interlayer coupling is due to van der Waals interactions are expected to be significantly weaker than the in-plane couplings J and are therefore neglected. The eigenvalues obtained from the model are $E_{\mathbf{q}}^{\pm} = v_S \pm |\gamma_{\mathbf{q}}|$, with $v_S = -(3JS + 2KS)$ and $\gamma_{\mathbf{q}} = JS\sum_j e^{i\mathbf{q}\cdot\mathbf{a}_j}$, where S is the spin [14,15]. With a wave vector of $\mathbf{q} = (H, H)$, where H is here used to parametrize the reciprocal lattice vector, the dispersion is quadratic for small H, $E \approx v_S \pm 3JS \pm 4\pi^2 JSH^2$. We fit Gaussian peaks to a series of constant energy cuts in the $(H, H, -2)$ plane through the MACS data to obtain the magnon dispersion. The exchange coupling can be determined from the prefactor $4\pi^2 JS$ of the quadratic term. Taking the reduced value of $S = 0.8(1)$, the fit

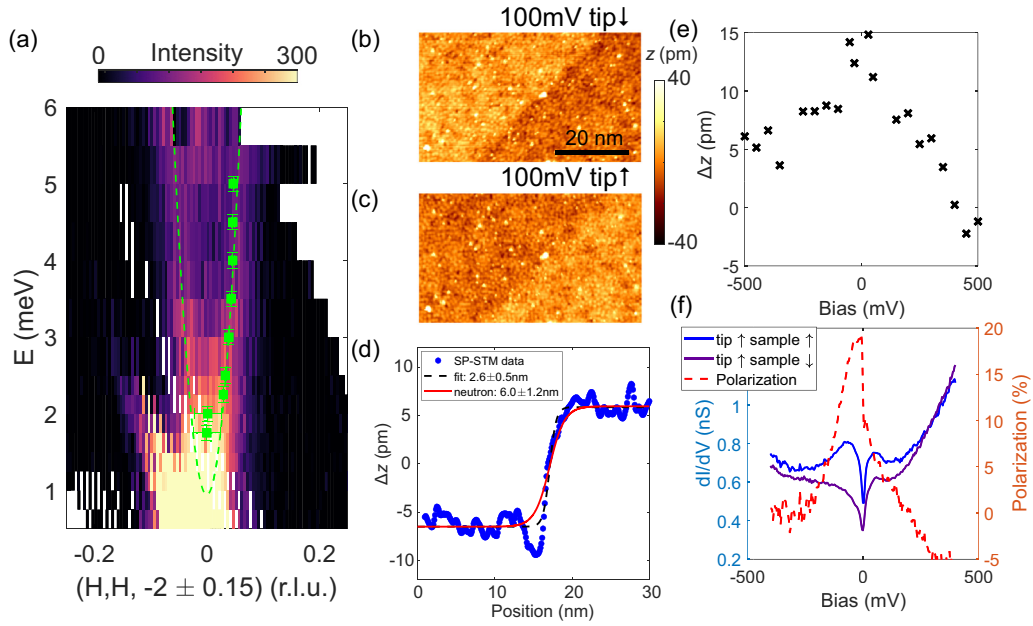

FIG. 3. Magnon dispersion and magnetic imaging. (a) Inelastic neutron scattering measurement of the spin-wave dispersion of Fe_3GeTe_2 around $\mathbf{q} = (H, H, -2)$ for $H = -0.2 \ldots 0.2$. The green line represents a parabolic fit to the data. The fit results in $J \approx 43(10)$ meV and $K \approx 0.6(1)$ meV (see main text for details). (b) A ferromagnetic domain wall imaged using spin-polarized STM ($V_s = 100$ mV, $I_s = 125$ pA). The domain wall runs diagonally through the image. (c) The same area as in (b) imaged with a spin-polarized tip with the opposite spin polarization from that used in (b) ($V_s = 100$ mV, $I_s = 125$ pA). (d) A line profile $z(x)$ taken through the difference of images (b) and (c) perpendicular to the domain wall. The red line shows the expected profile from the neutron scattering measurement. (e) The height difference Δz recorded between oppositely polarized areas as a function of applied bias voltage. (f) dI/dV spectra (blue curve) recorded on either side of the domain wall shown in (b) and (c) ($V_s = 400$ mV, $I_s = 250$ pA, $V_{\mathrm{mod}} = 3$ mV). The spectroscopy set point was chosen at a bias voltage where the domain wall was not visible. The resulting spin polarization determined from the dI/dV spectra is also shown (red curve).

yields $J \approx 43(10)$ meV and $K \approx 0.6(1)$ meV. The magnetic anisotropy is nonnegligible, which is consistent with previous reports [5,16], though somewhat smaller than the one reported previously from neutron scattering, whereas the exchange coupling is larger [17]. The difference in these values suggests a strong influence of the iron deficiency on the magnetic excitations: while our crystal has $y = 0.14$, the one studied by the authors of Ref. [17] had $y = 0.25$, almost two times that of our sample.

We can compare these values with the magnetic properties of the surface layer. Using spin-polarized STM [18,19] we were able to directly image ferromagnetic domain walls at the surface of Fe_3GeTe_2 [Fig. 3(b)]. The tip cluster was found to have a sufficiently small moment so that the tip magnetization can be switched by the magnetic interaction with the sample. Manipulating the tip magnetization in this way allowed us to image the same area with an oppositely polarized tip without having to apply an external magnetic field, which would at the same time move the domain wall and polarize the sample. Figure 3(c) shows an image with the same tip after the tip magnetization has flipped. By taking the difference of the images, we obtain an image of only the magnetic contrast [Fig. 3(d)]. From a line profile normal to the domain wall [Fig. 3(d)], we can analyze its width by fitting $z(x) = a + b\tanh[\pi(x - x_0)/\delta]$ to the data [18,20–23], assuming that the tip magnetization is parallel to the out-of-plane direction and reverses by 180° when changing its direction. We obtain a domain wall width of $\delta = 2.6 \pm 0.5$ nm. The domain wall width found here is smaller than that typically found in ferromagnetic films, which are usually on the order of 10–100 nm [22,23]. We can compare the domain wall width δ with the expected width δ_n using the exchange interaction J and magnetic anisotropy K obtained from neutron scattering through $\delta_n = \pi\sqrt{\frac{A}{K}}$ [24], where A is the exchange stiffness of the spins of the system being considered, which is related to the exchange interaction J. For a 2D hexagonal honeycomb lattice, this expression becomes $\delta_n = \pi d_{nn}\sqrt{\frac{3J}{4K}}$ [20,21] (see Supplemental Material S5 [32]), where d_{nn} is the nearest-neighbor distance between Fe atoms. By taking the values of J and K determined from the magnon dispersion in Fig. 3(a), we find a domain wall width $\delta_n = 6.0 \pm 1.2$ nm, which is somewhat larger than what is obtained from a fit to our spin-polarized STM measurement [see Fig. 3(d)]. We note, however, that visually, the domain wall profile suggested by neutron scattering appears very similar to the observed one. The smaller domain wall width which we observe at the surface suggests that the exchange coupling J is smaller in the surface layer compared to the bulk and the magnetic anisotropy K larger.

The apparent height of the domain wall in the spin-polarized STM images exhibits a strong dependence on the bias voltage. From images recorded at different bias voltages, we can determine how the spin polarization of the sample's electronic structure evolves with energy. For images recorded with a low bias voltage (<50 mV) the domain wall shows

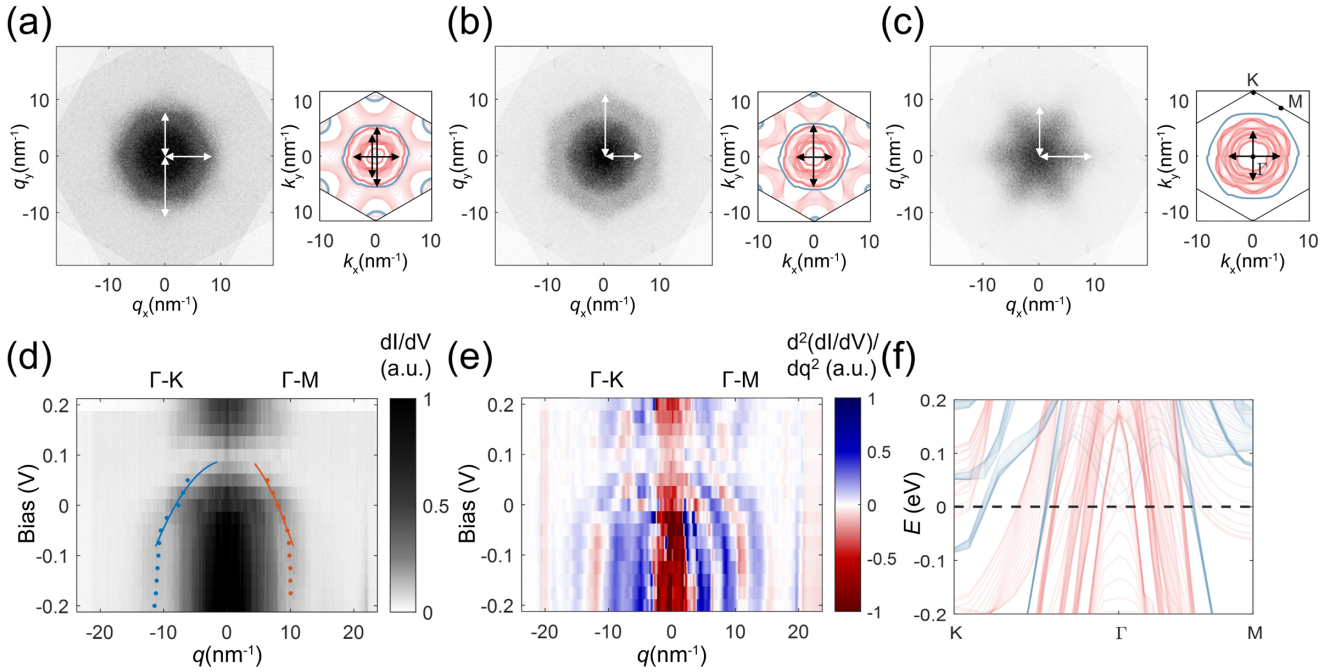

FIG. 4. Quasiparticle interference imaging. (a)–(c) Six-fold symmetrized FFT of the differential conductance $\tilde{g}(\mathbf{q}, V)$ and calculated constant energy contours, showing majority (red) and minority (blue) spin bands averaged over 16 k_z values from 0 to $2\pi/c$, at (a) 0 mV, (b) −60 mV, and (c) −300 mV. Corresponding scattering vectors are marked on the experimental data and band-structure calculation. (d) $\tilde{g}(\mathbf{q}, V)$ as a function of bias V for $\mathbf{q}$ along Γ-K and Γ-M taken from similar $\tilde{g}(\mathbf{q}, V)$ measurements to (a)–(c), averaged between $q_x/q_y = \pm 0.378$ nm^{-1} for Γ-K/Γ-M. Points fitted to the band dispersions along both directions are also plotted, with parabolic fits to the highest four energy points for each direction giving an average effective mass of $m^* = 5.3 \pm 0.8\, m_e$ (Γ-M: $4.5\, m_e$, Γ-K: $6.1\, m_e$). (e) Second derivative with respect to $\mathbf{q}$ of the differential conductance map, $\frac{\partial^2 \tilde{g}(\mathbf{q},V)}{\partial q^2}$, as a function of bias for $\mathbf{q}$ along Γ-K and Γ-M. The $\tilde{g}(\mathbf{q}, V)$ data were smoothed along the $\mathbf{q}$-direction with a window of 5.060 nm^{-1} before calculating the second derivative. (f) DFT calculation of the band structure of Fe_3GeTe_2, showing majority (red) and minority (blue) spin bands averaged over 16 k_z values from 0 to $2\pi/c$.

the largest contrast. As the bias voltage is increased the magnetic contrast decreases and disappears at 400 mV before reversing at even higher bias values. For negative applied bias the magnetic contrast remains more or less constant. By recording STS spectra on either side of the domain wall (hence with different magnetization directions of the sample) with a set point condition where the domain wall is not visible it is possible to extract the spin polarization as a function of bias voltage. The spectra recorded on either side of the domain wall are shown in Fig. 3(f). The polarization can be extracted from the spectra using the relation $P = \frac{g_{\uparrow\uparrow}(V) - g_{\uparrow\downarrow}(V)}{g_{\uparrow\uparrow}(V) + g_{\uparrow\downarrow}(V)}$ [18,19] [Fig. 3(f)]. The spin polarization shows a sharp peak of up to 20% spin polarization just below the Fermi level at an energy of -43 ± 6 mV.

C. Quasiparticle interference

To characterize the interplay between magnetism and the electronic structure, we used quasiparticle interference imaging. Figures 4(a) to 4(c) show the Fourier transform of quasiparticle interference maps $\tilde{g}(\mathbf{q}, V)$ at three different bias voltages (0 mV, −60 mV, and −300 mV), with the calculated band structure in the first Brillouin zone for comparison, integrated over k_z. There are clear hexagonal features in the experimental data, marked with arrows, with equivalent scattering vectors shown in the calculated band structure. All of the vectors observed experimentally can be assigned to scattering processes between bands with majority spin character. These bands are also the ones which exhibit a more 2D character, as represented by the opacity in the calculation. Despite being strongly 2D, the minority band centered around the Γ point is not visible in any of our measurements. The DFT calculations show that the spin-minority bands have predominantly iron character with little weight on the outermost Te atoms, whereas the majority bands have Te character, suggesting that we fail to detect the minority band due to matrix element effects.

A cut of the differential conductance along K-Γ-M in the 2D Brillouin zone is shown in Fig. 4(d) between −200 mV and +200 mV. From the quasiparticle interference (QPI) cuts we can extract the properties of the hole-like band that crosses the Fermi level. By fitting a parabolic dispersion, Fig. 4(d), and assuming that it is due to intraband scattering, we determine that it has an effective mass $m^* = 5.3 \pm 0.8\, m_e$ and a Fermi wave vector $k_f = 4.1 \pm 0.3$ nm^{-1} along Γ–K (8.2 nm^{-1} in q-space), which is in approximate agreement with that of a hexagonal pocket centered around Γ seen in ARPES measurements [7,12,25]. From the fits we find a band maximum at 106 ± 25 mV above the Fermi level. To highlight sharp features, the second derivative with respect to $\mathbf{q}$ of the smoothed dI/dV data is plotted in Fig. 4(e). In these, the hole

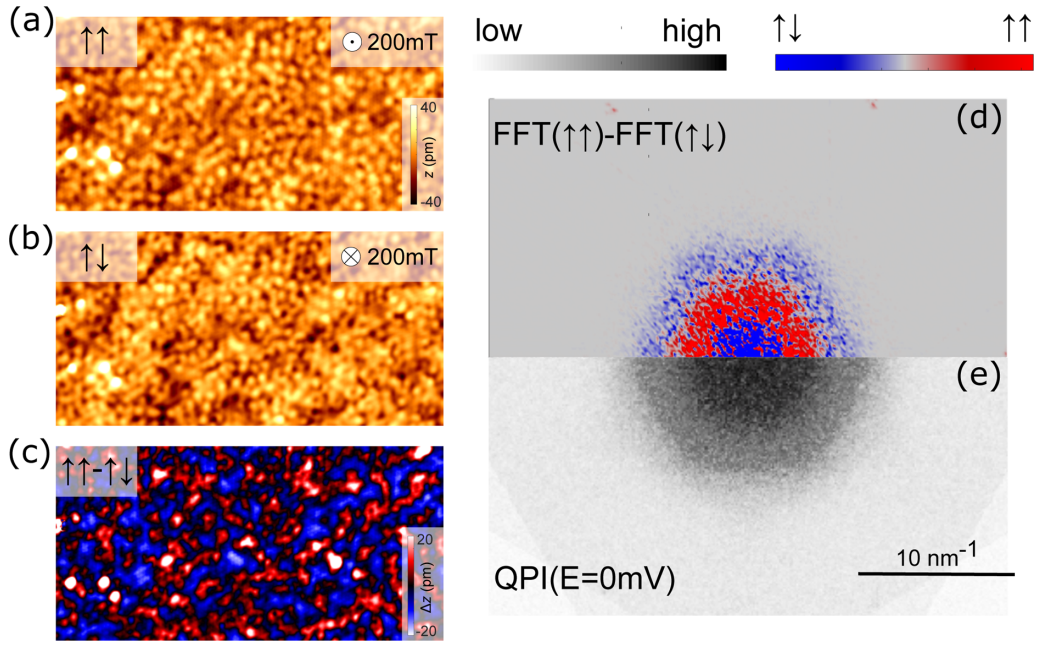

FIG. 5. Spin-polarized quasiparticle interference. (a) SP-STM image (30 mV, 100 pA, 41 × 20 nm^2) recorded with the tip polarized parallel to the sample by applying a 200 mT field along the sample c axis. (b) Image of the same location with the same tip after the magnetization of the tip was reversed relative to the sample by applying a 200 mT field antiparallel to the sample c axis. Slight differences in the topographic contrast can be observed. (c) The difference of (a) and (b). Subsurface Fe clusters become apparent in the difference image. (d) The quasiparticle interference pattern recorded at the Fermi level ($V = 0$ V). (e) Difference of the Fourier transform of topographies ($V_s = 30$ mV, $I_s = 100$ pA) recorded with opposite relative tip and sample spin orientations. Red vectors show up more intensely when the magnetization of tip and sample are parallel, and blue regions when they are antiparallel with respect to each other, showing the different spin-character of the bands.

band is more readily observed with a maximum at around 150 mV at the Γ point. We assign this band to the 2D band at the same energy in the calculated k_z-integrated band structure, Fig. 4(f).

Using a spin-polarized tip allows to determine the spin character of the different bands. To this end, we undertook spin-polarized topographic imaging as a function of applied field. The relative orientation of the tip and sample magnetizations will switch at different fields [see Figs. 5(a) to 5(c)], enabling imaging of the quasiparticle scattering with parallel and antiparallel alignment of their magnetizations. We observe a significant change in the topographic contrast when the tip and sample are not magnetized in the same direction anymore. Taking the difference of the Fourier transforms of topographies with parallel and antiparallel magnetization [Fig. 5(d)] reveals strong changes in the relative intensity of the scattering vectors. By comparing the Fourier transform with the QPI mapping at the Fermi level [Fig. 5(e)] we determine that the observed magnetic contrast is due to the spin-dependent imaging of Friedel oscillations between differently polarized bands at the Fermi level and thus reveals information about the spin polarization of the bands in the vicinity of the Fermi energy.

III. DISCUSSION

Our study of Fe_3GeTe_2 provides new insights from relating microscopic information obtained from low-temperature scanning tunneling microscopy to bulk properties obtained from neutron scattering. We find that in the surface layer, the magnetic properties deviate slightly from those in the bulk, as might be expected from the three-dimensional nature of some parts of the electronic structure. A comparison of the imaging of domain walls with the magnetic exchange interaction J and anisotropy K obtained from neutron scattering reveal a surprisingly good agreement. One would expect the ratio K/J to be slightly larger for the surface layer compared to the bulk due to a larger magnetic anisotropy and smaller exchange coupling: the smaller coordination number of atoms in the surface layer will lead to a decreased exchange energy J, while at the same time the lower symmetry is expected to result in a larger anisotropy K. It is well known from a number of systems that the magnetic anisotropy increases with reduced dimensionality [26]. The reduction in J in the surface layer is consistent with the lower Curie temperature T_C found in thin films and in the monolayer limit, where T_C is suppressed significantly [4,5]. This system therefore confirms the previously observed trend that, while the surface of a magnetic bulk material does not exhibit radically different magnetic properties, there are subtle differences [27].

From band-structure calculations, we find that the Fermi surface is dominated by bands of spin majority character with significant k_z-dispersion and quasi-2D bands of spin minority character. A comparison with quasiparticle interference imaging reveals dominant wave vectors, which are broadly consistent with the band-structure calculations. We use spin-polarized imaging to determine the spin-polarization of the bands near the Fermi energy, and find, consistent with the calculations, a hexagonal ring of scattering which we attribute to the bands with spin-majority character embedded in a

rather broad distribution of electronic states with opposite spin character. While a more quantitative comparison, using, e.g., a continuum calculation of the local density of states to model the quasiparticle interference [28] would be desirable, we expect that the large amount of scattering due to the iron deficiency and three-dimensionality of some of the bands will result in rather broad features [29,30], as observed in the experiment—and therefore not provide significant additional insight here.

Underpinning data will be made available at University of St Andrews Research Portal [31].

ACKNOWLEDGMENTS

C.T. and P.W. acknowledge funding through Grants No. EP/R031924/1 and No. EP/T031441/1, L.C.R. through the Royal Commission for the Exhibition of 1851, I.B. through the International Max Planck Research School for Chemistry and Physics of Quantum Materials, and H.L. through the ISIS facility development studentship program. Access to MACS was provided by the Center for High Resolution Neutron Scattering, a partnership between the National Institute of Standards and Technology and the National Science Foundation under Agreement No. DMR-1508249.

[1] J. He, S. Li, A. Bandyopadhyay, and T. Frauenheim, Nano Lett. **21**, 3237 (2021).
[2] C. Gong, L. Li, Z. Li, H. Ji, A. Stern, Y. Xia, T. Cao, W. Bao, C. Wang, Y. Wang, Z. Q. Qiu, R. J. Cava, S. G. Louie, J. Xia, and X. Zhang, Nature (London) **546**, 265 (2017).
[3] B. Huang, G. Clark, E. Navarro-Moratalla, D. R. Klein, R. Cheng, K. L. Seyler, D. Zhong, E. Schmidgall, M. A. McGuire, D. H. Cobden, W. Yao, D. Xiao, P. Jarillo-Herrero, and X. Xu, Nature (London) **546**, 270 (2017).
[4] Z. Fei, B. Huang, P. Malinowski, W. Wang, T. Song, J. Sanchez, W. Yao, D. Xiao, X. Zhu, A. F. May, W. Wu, D. H. Cobden, J.-H. Chu, and X. Xu, Nat. Mater. **17**, 778 (2018).
[5] Y. Deng, Y. Yu, Y. Song, J. Zhang, N. Z. Wang, Z. Sun, Y. Yi, Y. Z. Wu, S. Wu, J. Zhu, J. Wang, X. H. Chen, and Y. Zhang, Nature (London) **563**, 94 (2018).
[6] M. Costa, N. M. R. Peres, J. Fernández-Rossier, and A. T. Costa, Phys. Rev. B **102**, 014450 (2020).
[7] Y. Zhang, H. Lu, X. Zhu, S. Tan, W. Feng, Q. Liu, W. Zhang, Q. Chen, Y. Liu, X. Luo, D. Xie, L. Luo, Z. Zhang, and X. Lai, Sci. Adv. **4**, eaao6791 (2018).
[8] A. F. May, S. Calder, C. Cantoni, H. Cao, and M. A. McGuire, Phys. Rev. B **93**, 014411 (2016).
[9] X. Kong, G. D. Nguyen, J. Lee, C. Lee, S. Calder, A. F. May, Z. Gai, A.-P. Li, L. Liang, and T. Berlijn, Phys. Rev. Materials **4**, 094403 (2020).
[10] H.-J. Deiseroth, K. Aleksandrov, C. Reiner, L. Kienle, and R. K. Kremer, European J. Inorganic Chem. **2006**, 1561 (2006).
[11] C.-K. Tian, C. Wang, W. Ji, J.-C. Wang, T.-L. Xia, L. Wang, J.-J. Liu, H.-X. Zhang, and P. Cheng, Phys. Rev. B **99**, 184428 (2019).
[12] K. Kim, J. Seo, E. Lee, K.-T. Ko, B. S. Kim, B. G. Jang, J. M. Ok, J. Lee, Y. J. Jo, W. Kang, J. Hoon Shim, C. Kim, H. Woong Yeom, B. I. Min, B.-J. Yang, and J. S. Kim, Nat. Mater. **17**, 794 (2018).
[13] S. W. Lovesey, *Theory of Neutron Scattering From Condensed Matter* (Clarendon, London, 1984).
[14] S. A. Owerre, J. Phys.: Condens. Matter **28**, 386001 (2016).
[15] S. S. Pershoguba, S. Banerjee, J. C. Lashley, J. Park, H. Ågren, G. Aeppli, and A. V. Balatsky, Phys. Rev. X **8**, 011010 (2018).
[16] C. Tan, J. Lee, S.-G. Jung, T. Park, S. Albarakati, J. Partridge, M. R. Field, D. G. McCulloch, L. Wang, and C. Lee, Nat. Commun. **9**, 1554 (2018).
[17] S. Calder, A. I. Kolesnikov, and A. F. May, Phys. Rev. B **99**, 094423 (2019).
[18] R. Wiesendanger, Rev. Mod. Phys. **81**, 1495 (2009).
[19] M. Bode, Rep. Prog. Phys. **66**, 523 (2003).
[20] R. Moreno, R. F. L. Evans, S. Khmelevskyi, M. C. Muñoz, R. W. Chantrell, and O. Chubykalo-Fesenko, Phys. Rev. B **94**, 104433 (2016).
[21] A. Aharoni, *Introduction to the Theory of Ferromagnetism*, International Series of Monographs on Physics (Clarendon, New York, 2000).
[22] L. Berbil-Bautista, S. Krause, M. Bode, and R. Wiesendanger, Phys. Rev. B **76**, 064411 (2007).
[23] R. Ravlić, M. Bode, A. Kubetzka, and R. Wiesendanger, Phys. Rev. B **67**, 174411 (2003).
[24] S. Blundell, *Magnetism in Condensed Matter* (Oxford University Press, New York, 2001), includes bibliographical references and index.
[25] X. Xu, Y. W. Li, S.R. Duan, S. L. Zhang, Y. J. Chen, L. Kang, A. J. Liang, C. Chen, W. Xia, Y. Xu, P. Malinowski, X. D. Xu, J. H. Chu, G. Li, Y. F. Guo, Z. K. Liu, L. X. Yang, and Y. L. Chen, Phys. Rev. B **101**, 201104(R) (2020).
[26] P. Gambardella, Science **300**, 1130 (2003).
[27] C. Trainer, M. Songvilay, N. Qureshi, A. Stunault, C. M. Yim, E. E. Rodriguez, C. Heil, V. Tsurkan, M. A. Green, A. Loidl, P. Wahl, and C. Stock, Phys. Rev. B **103**, 024406 (2021).
[28] A. Kreisel, C. A. Marques, L. C. Rhodes, X. Kong, T. Berlijn, R. Fittipaldi, V. Granata, A. Vecchione, P. Wahl, and P. J. Hirschfeld, npj Quantum Mater. **6**, 100 (2021).
[29] L. C. Rhodes, M. D. Watson, T. K. Kim, and M. Eschrig, Phys. Rev. Lett. **123**, 216404 (2019).
[30] C. A. Marques, M. S. Bahramy, C. Trainer, I. Marković, M. D. Watson, F. Mazzola, A. Rajan, T. D. Raub, P. D. C. King, and P. Wahl, Nat. Commun. **12**, 6739 (2021).
[31] C. Trainer, O. Armitage, H. Lane, L. Rhodes, E. Chan, I. Benedičič, J. Rodriguez-Rivera, O. Fabelo, C. Stock, and P. Wahl, Underpinning data for "Relating spin-polarized STM imaging and inelastic neutron scattering in the van-der-Waals ferromagnet Fe_3GeTe_2", University of St Andrews Research Portal, https://doi.org/10.17630/0f5919b0-dc32-4940-bf34-561aca5c9a4b (2022).
[32] See Supplemental Material at http://link.aps.org/supplemental/10.1103/PhysRevB.106.L081405 for more information.